Article

Exploring Heterointerface Characteristics and Charge-Storage Dynamics in ALD-Developed Ultra-Thin TiO_2-In_2O_3/Au Heterojunctions

Mohammad Karbalaei Akbari [1,2,*], Nasrin Siraj Lopa [1,2] and Serge Zhuiykov [1,2]

[1] Department of Solid-State Sciences, Faculty of Science, Ghent University, Krijgslaan 281/S1, B-9000 Ghent, Belgium; nasrin.lopa@ghent.ac.kr (N.S.L.); sereg.zhuiykov@ghent.ac.kr (S.Z.)
[2] Center for Green Chemistry & Environmental Biotechnology, Ghent University Global Campus, Incheon 21985, Republic of Korea
* Correspondence: mohammad.akbari@ugent.be

Abstract: Directional ionic migration in ultra-thin metal-oxide semiconductors under applied electric fields is a key mechanism for developing various electronic nanodevices. However, understanding charge transfer dynamics is challenging due to rapid ionic migration and uncontrolled charge transfer, which can reduce the functionality of microelectronic devices. This research investigates the supercapacitive-coupled memristive characteristics of ultra-thin heterostructured metal-oxide semiconductor films at TiO_2-In_2O_3/Au Schottky junctions. Using atomic layer deposition (ALD), we nano-engineered In_2O_3/Au-based metal/semiconductor heterointerfaces. TEM studies followed by XPS elemental analysis revealed the chemical and structural characteristics of the heterointerfaces. Subsequent AFM studies of the hybrid heterointerfaces demonstrated supercapacitor-like behavior in nanometer-thick TiO_2-In_2O_3/Au junctions, resembling ultra-thin supercapacitors, pseudocapacitors, and nanobatteries. The highest specific capacitance of 2.6×10^4 $F.g^{-1}$ was measured in the TiO_2-In_2O_3/Au junctions with an amorphous In_2O_3 electron gate. Additionally, we examined the impact of crystallization, finding that thermal annealing led to the formation of crystalline In_2O_3 films with higher oxygen vacancy content at TiO_2-In_2O_3 heterointerfaces. This crystallization process resulted in the evolution of non-zero I-V hysteresis loops into zero I-V hysteresis loops with supercapacitive-coupled memristive characteristics. This research provides a platform for understanding and designing adjustable ultra-thin Schottky junctions with versatile electronic properties.

Keywords: atomic layer deposition; heterostructured metal oxides; charge-storage dynamic; supercapacitors; scanning capacitance microscope; memristors

Citation: Karbalaei Akbari, M.; Lopa, N.S.; Zhuiykov, S. Exploring Heterointerface Characteristics and Charge-Storage Dynamics in ALD-Developed Ultra-Thin TiO_2-In_2O_3/Au Heterojunctions. *Coatings* **2024**, *14*, 880. https://doi.org/10.3390/coatings14070880

Academic Editor: Amin Bahrami

Received: 28 May 2024
Revised: 10 July 2024
Accepted: 12 July 2024
Published: 14 July 2024

Copyright: © 2024 by the authors. Licensee MDPI, Basel, Switzerland. This article is an open access article distributed under the terms and conditions of the Creative Commons Attribution (CC BY) license (https://creativecommons.org/licenses/by/4.0/).

1. Introduction

Semiconductor nanoelectronic devices are continuously advancing to meet the growing demand for low-power electronic functional systems. Atomic layer deposition (ALD) is a powerful technique for the conformal deposition of semiconductor oxide films, providing highly precise thickness control over geometrically complex substrates [1,2]. ALD is a precise tool for heterointerface engineering of ultra-thin heterostructured metal-oxide semiconductors, which are used in various electronic nanodevices. It enables the design and fabrication of functional semiconductor heterointerfaces with two-dimensional (2D) characteristics [1]. Additionally, this technique facilitates the functionalization, doping, and growth of nanostructures for energy storage and nanoelectronic applications, such as supercapacitors [2]. ALD is also effective for designing and fabricating ultra-thin semiconductor heterostructures with atomically sharp two-dimensional interfaces [3,4]. This advanced thin-film fabrication technique has enabled the creation of a wide range of atomically thin heterostructured semiconductors. Particularly, plasma-enhanced atomic layer deposition

(PE-ALD) facilitates low-temperature growth of amorphous, crystalline, and metastable phases with desired properties, due to using high-energy ionized plasma [5–7].

This fabrication technique provides the platform for fabrication of ultra-thin semiconductors allowing precise control over the migration of electrical charges through electronically modulated heterointerfaces [8]. Additionally, PE-ALD offers a broad selection of materials for the deposition of semiconductor components, enabling tunable electronic characteristics. PE-ALD is acknowledged as a highly capable technique with atomic-scale precision, ideal for developing large-area heterostructured films. This method enables the functional creation and engineering of ultra-thin heterointerfaces in electronic systems, making such advancements practically achievable. The precise design of ultra-thin heterostructured semiconductor materials opens extensive opportunities for modulating the electronic structure of nanoelectronic devices [9]. In particular, a conceptually simple structure—an ultra-thin semiconductor layer sandwiched between two conductive channels—can exhibit the outstanding functionalities [10,11].

Despite significant developments, there is still a lack of proper understanding regarding the modulation of charge transfer phenomena in the electron channels of semiconductor resistive switching layers [12]. Controlling storage and transfer in these few-nanometer-thick electron channels is the primary mechanism for designing various electronic systems. In particular, the development of hybrid nanoelectronic adjustable gates significantly enhances device performance, paving the way for the fabrication of atomically thin sensors, neural receptors [13], nanobatteries [14], supercapacitors [15], memristors [16], and artificial synaptic junctions [17,18]. Among the various characteristics of nanoelectronic gates, the capacitive-coupled memristive behavior of sandwiched ultra-thin semiconductor layers is the origin of intriguing properties and phenomena, which require further exploration to be fully understood. ALD provides the opportunity to fundamentally design programmable heterointerfaces and integrate them into functional devices. It also offers a supplementary mechanism for investigating low-power charge transfer phenomena in ultra-thin electronic channels. Furthermore, the effects of the characteristics of ALD films, including crystallinity and heterointerface characteristics, should be investigated to understand the mechanism of charge transfer in heterostructured metal-oxide semiconductors. It is worth mentioning that the low-temperature ALD process results in the growth of mostly amorphous or a mixture of amorphous and crystalline structures. Therefore, it is technically and scientifically important to investigate the influence of electron gates at metal/semiconductor heterojunctions and to elaborate on the charge transfer mechanisms in ultra-thin metal-oxide nanoelectronic devices.

The present study investigates the design and fabrication of adjustable Schottky junctions, where the heterointerface between an Au substrate and a TiO_2 semiconductor component is modified by incorporating an additional ultra-thin semiconductor interlayer. TiO_2 is a well-known semiconductor with recognized memristive characteristics [19,20], where ionic migration is the primary mechanism of charge transfer and resistive switching, resulting in distinctive resistive switching behavior with a zero I-V curve configuration. In this study, PE-ALD was employed to deposit In_2O_3 channels as a gate material between the Au substrate and TiO_2. In_2O_3 is one of the interesting metal-oxide semiconductors with rich electronic structure. The significant electronic characteristics of In_2O_3 provides various opportunities for application of In_2O_3 in transparent infrared optoelectronic systems, storage systems, and batteries [21]. Particularly, In_2O_3 doping and its heterointerface engineering provides the opportunity for development of transparent thin conductive films, with superior chemical stability for various types of photonic and energy applications [22]. High-temperature thermal ALD of In_2O_3 films can lead to unwanted reactions and precursor decomposition, resulting in pore formation or island growth of the films. Consequently, thermal annealing restricts the successful conformal deposition of In_2O_3 films in high aspect ratio structures and causes thickness non-uniformities. To address these issues, we utilized a previously developed PE-ALD recipe for the deposition of ultra-thin In_2O_3 films in the present study [23].

We specifically examined the impact of crystallinity on the charge transfer mechanism at the heterointerfaces, focusing on both crystalline (c) and amorphous (α) structures of In_2O_3 films. To observe the I-V hysteresis and C-V characteristics of TiO_2-In_2O_3/Au Schottky junctions, we employed conductive atomic force microscopy (c-AFM) and scanning capacitance microscopy (SCM). The versatile and precise c-AFM measurements demonstrated the role of the electric channel in the supercapacitive-coupled memristive behavior of the TiO_2-In_2O_3 heterostructure. We observed a transition from fully supercapacitive states in amorphous In_2O_3 (α) channels at the TiO_2-In_2O_3 heterointerfaces to memristive states in crystalline In_2O_3 (c) channels. A specific capacitance of 2.6×10^4 $F.g^{-1}$ was measured via SCM in studies of In_2O_3 (α)-TiO_2 heterostructures. Therefore, this study provides foundational knowledge and evidence for the development of tunable TiO_2-In_2O_3/Au heterojunctions, aimed at modulating adaptable electronic channels for desired solid-state applications.

2. Materials and Methods

To fabricate the heterostructured semiconductor films, 150 nm Au crystalline film was deposited by electronbeam evaporation technique on Si/SiO_2 substrate. The 150 nm CVD SiO_2 film was deposited on Si substrate to prevent the current leakage from the Au film to the Si substrate. The 10 nm-thick Cr film was used as the adhesion layer between the Au and Si/SiO_2 sublayers. PE-ALD was used to deposit ~5.0 nm-thick indium oxide films over Au electrodes. The b-diketonate tris (2,2,6,6-tetramethyl-3,5-heptanedionato) indium (III), [In-(TMHD)3], as indium precursors, and O_2 plasma as the reactant were used for the deposition of In_2O_3 in a N_2 atmosphere at 150 °C. A typical PE-ALD cycle is a 20 s process including 5 pulse times for both precursors, reactant and plasma, followed by a 5 s evacuation time after each pulse. The in situ ellipsometry was employed to monitor the growing thickness of In_2O_3 film (SE, J. A. Woollam M-2000). To this aim, samples were deposited on the 5.0 in diameter Si/SiO_2/Au wafers, and the ellipsometry thickness map of the ALD films was monitored and measured after the PE-ALD process to confirm the thickness uniformity of the ALD films. Finally, the wafers were diced into 1 cm^2 square samples for the following materials characterization and electrical measurement studies. In one group of samples, the as-deposited In_2O_3 films were later thermally annealed under a controlled atmosphere (N_2 atmosphere for 10 min at 450 °C at a rate of 60 °C min^{-1}). After the thermal treatment, the 19.0 nm-thick TiO_2 films were deposited via PE-ALD (tetrakis dimethylamino titanium and O_2 plasma) over the indium oxide films. In the PE-ALD process of TiO_2, the TDMAT and O_2 plasma durations were set at 0.1 s and 0.6 s, respectively. X-ray photoelectron spectroscopy (XPS, Thermo Scientific theta probe, MA, USA) was employed to analyze the chemical states and to measure the valance band maximum (VBM) of heterostructured TiO_2- In_2O_3 films on Au substrates. High-resolution X-ray diffraction (HR-XRD, (SmartLab, Rigaku) was employed to investigate the structure of ALD films before and after thermal treatments. The nanostructural analysis was performed by transmission electron microscope (TEM, JEM-ARM 200F-NEOARM). The lamella samples of heterointerfaces were fabricated by a precise focused ion beam system (FIB focused ion beam—Crossbeam 540). The chemical analyses of atomically thin heterointerfaces were performed by the energy dispersive spectrometer (EDS) of a TEM machine.

AFM (Park-NX10) was employed in pin-point mode. In the c-AFM studies, the ALD films were investigated by the Cr-Pt-Ir tip of c-AFM machine, featuring a radius curvature of approximately 15.0 nm, a stiffness of 0.20 Nm^{-1}, and a resonance frequency of 25.0 kHz during measurements. The I-V characteristics of the hybrid interfaces were subsequently measured by nano-positioning the conductive cantilever probe at a fixed location on the surface of 2D films. Samples were kept in an inert Ar atmosphere before c-AFM studies, followed by electrical measurements under flow of Ar gas in the enclosed measurement chamber of the AFM machine. The current maps of thin films were monitored during in situ characterization of the dynamic charge transfer. To investigate the supercapacitive character-

istics of the TiO_2-In_2O_3/Au films, scanning capacitance microscope (SCM) was employed, which is a powerful AFM technique for the characterization of semiconductor devices.

3. Results

3.1. Materials Characterization

The precise design of electronic channels fundamentally affects the performance of nanoelectronic devices. Indium oxide is a well-known transparent conducting oxide (TCO) with a network of polyhedral structures [24]. The fundamental characteristics of the electronic band structure of a TCO semiconductor originate from the interaction of metal–oxygen pairs [24]. The microstructural characteristics of indium oxide govern its electronic properties, particularly the mechanisms of charge transfer and charge storage in ultra-thin metal-oxide films. It is worth mentioning that the considerable increase in non-lattice oxygen following the annealing process is expected to result in increased conductance of the system. The transition from amorphous to crystalline structure alters the charge transport regimes in the InO_x film. In amorphous InO_x nanostructures, localization is the primary transport mechanism. As the structure transitions from fully amorphous to mixed amorphous/crystalline, and finally to fully crystalline, the charge transport mechanism changes accordingly. Initially, localization dominates in the amorphous structure, then transitions to hopping, multi-phase percolation, scattering, and ultimately to bulk conductivity in the fully crystalline structure. In the present study, the amorphous In_2O_3 (α) and crystalline In_2O_3 (c) channels were employed as ultra-thin channels for the TiO_2 resistive switching layer (Figure 1a). The amorphous In_2O_3 has a non-periodic and mostly distorted polyhedral structure [25]. The composition and bonding structures of cations in indium oxide determine the characteristics of electron localization and the parameters of variable range hopping [25]. The limit of carrier mobility is determined by the robustness of In-O bonding chains in the nanostructure of amorphous oxide semiconductors. In amorphous indium oxide, the nearest In-O bonds are clearly defined in short-range order, while longer-range order is missing. In amorphous InO_x, the polyhedral structures are linked together either at their edges, corners, or faces [24]. In edge-sharing, two oxygens are shared between two polyhedral structures, while in corner-sharing, the polyhedral structures share one oxygen atom between two corners. In the least common structures, polyhedrons share three or more oxygen atoms, forming a face-sharing configuration [23]. The non-shared polyhedral indium oxide is another possible structural coordination of In-O bindings (Figure 1b). The structural distortion in this amorphous semiconductor oxide originates from the weak ionic bonding between atomic oxygens and the spherical s-orbitals of the indium atoms [24–26]. The stoichiometric characteristics of oxygen atoms determine the generation of free electrons in amorphous In_2O_3. Particularly, the metal/oxygen ratio governs the formation of structural defects at metal-oxide structures at their band edges. Previous studies confirmed that a crystalline-to-amorphous transition is accompanied by a reduction in In-O coordination, where over 25% of the indium atoms have a coordination number of five or less [24]. Therefore, the concentration and degree of localization of conduction defects caused by the oxygen stoichiometric characteristics play an important role in the charge transfer mechanism in indium oxide. Figure 1c depicts the O 1s XPS spectrum of the as-deposited In_2O_3 film after 30 s of ion milling (18.26%). The peak at 529.3 eV corresponds to In-O bonding in the lattice of the In_2O_3 structure (81.6%), while the peak at 530.2 eV is assigned to non-lattice oxygen in the amorphous In_2O_3 structure [27,28]. We further investigated the O 1s spectrum of the In_2O_3 film after rapid thermal annealing (Figure 1d). The samples were ion milled to reach the In_2O_3/Au heterointerfaces. Consequently, the intensity of characteristic peaks of non-lattice oxygen at 531.3 eV is considerably higher than that of the lattice oxygen. After the deposition of TiO_2 films at 150°C, XPS measurements were conducted again. Consequently, the O 1s spectra of TiO_2-In_2O_3 (α) and TiO_2-In_2O_3 (c) heterostructured films were investigated. The results are respectively presented in Figure 1e,f. The characteristic O 1s peaks of lattice oxygen and non-lattice oxygen are observed at 529.8 eV and 530.5 eV, respectively, in

heterostructured films. Notably, both peaks represent similar O 1s XPS characteristics at the same measurement depth, confirming the analogous chemical states at the TiO_2-In_2O_3 (α) and TiO_2-In_2O_3 (c) heterostructures.

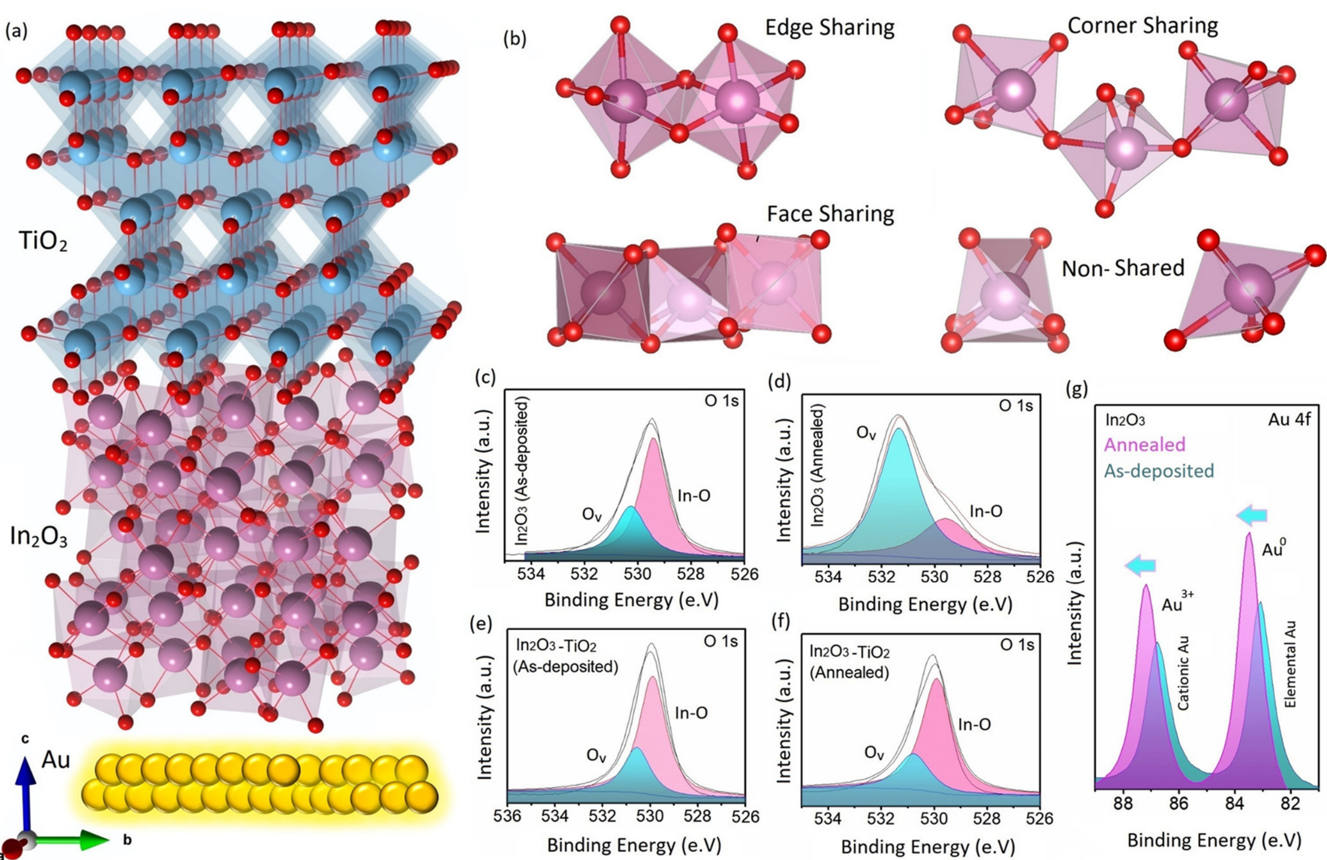

Figure 1. (**a**) Illustrates the atomic-scale graphical representation of the TiO_2- In_2O_3/Au heterostructure; (**b**) the atomic-scale graphical depiction of polyhedral In-O-In bonds within the amorphous In_2O_3 structure. Additionally, it presents the O 1s XPS spectra of (**c**) as-deposited In_2O_3; (**d**) the annealed In_2O_3; (**e**) the as-deposited TiO_2-In_2O_3; and (**f**) In_2O_3 (annealed)-TiO_2 films. (**g**) The Au 4f XPS spectra of In_2O_3/Au heterointerfaces, before and after thermal annealing.

The XPS results confirm the alteration of chemical states at the In_2O_3/Au heterointerfaces after thermal annealing at 450 °C. The increased values of structural vacancies are attributed to the interaction between the sublayer and the In_2O_3 ultra-thin film. The interaction between the Au sublayer and the ultra-thin In_2O_3 film was investigated using the XPS method. Figure 1g represents the Au 4f XPS spectra of the In_2O_3-Au heterointerfaces before and after thermal annealing. Two distinct peaks corresponding to elemental Au^0 and metal cationic Au^{3+} were detected in the XPS results (Figure 1g). We further investigated the collective data of the Au 4f and In 3d spectra before and after thermal annealing at the In_2O_3/Au heterointerfaces. The comparison of the collective data shows the composition at the In_2O_3/Au heterointerfaces. Before thermal annealing, the collective amounts of 1.54 at. % of Au^0, 1.26 at. % of Au^{3+}, and 5.3 at. % of In were characterized at the heterointerfaces [29,30]. After thermal annealing, these collective values changed to 0.21 at. %, 0.18 at. %, and 0.21 at. %, respectively, for metallic Au (Au^0), Au^{3+}, and In. It is worth mentioning that we neglected the amounts of adsorbed gases and carbonaceous residue. The recognizable shift of Au 4f to higher binding energies after thermal annealing confirms the alteration of the oxidation state of Au atoms at the heterointerfaces. We further investigated the Au 4f spectra of TiO_2-In_2O_3/Au heterojunctions before and after thermal annealing. A similar shift of Au 4f peaks to higher binding energies was observed. These observations can be attributed to the elemental distribution and the substitution of

atoms by vacancies at the In_2O_3/Au heterojunctions or one of the sublattices. It can also be attributed to the crystallographic reorientation of sublayer Au granular films and the mutual elemental diffusion at In_2O_3/Au heterointerfaces during the annealing process. Therefore, we precisely observed the heterointerfaces using a high-resolution transmission electron microscope and XPS techniques.

Regarding the capability of plasma-enhanced ALD (PE-ALD) for conformal wafer-scale deposition of ultra-thin heterostructured semiconductors, it is crucial to characterize the material properties of the heterointerfaces developed in our setup. Characterizing these heterointerfaces in ultra-thin heterojunctions is fundamentally important for understanding the mechanisms of charge-storage dynamics and memristive characteristics in these functional semiconductor devices. To this end, the material structure and chemical composition of TiO_2-In_2O_3 heterointerfaces were investigated using high-resolution transmission electron microscopy (HR-TEM), X-ray photoelectron spectroscopy (XPS), X-ray diffraction (XRD), and Raman spectroscopy. Figure 2 represents the results of TEM studies on the TiO_2-In_2O_3 heterointerfaces. Figure 2a depicts a typical high-magnification cross-sectional view of the heterojunctions. It appears that the ALD process resulted in wafer-scaled conformal deposition of heterostructured metal-oxide films on an Au substrate (Figure 2a). The TEM studies demonstrate an ultra-thin heterostructured film characteristic of amorphous In_2O_3 ALD film before the annealing process. Figure 2b shows a high-resolution image of the as-deposited ALD films with an ultra-smooth, sharp heterointerface, which is characteristic of amorphous metal-oxide films. The corresponding SAED patterns from the ALD films represent halo diffusive patterns (Figure 2b), indicating the semi-amorphous nature of the as-deposited ALD film. We further investigated the cross-sectional TEM image of TiO_2-In_2O_3 heterointerfaces (Figure 2c), where distinguishable borders are observed between the crystalline In_2O_3 (c) and amorphous TiO_2 structures. In this sample, the In_2O_3 films were annealed. Subsequently, the top-layer TiO_2 film was deposited on crystalline In_2O_3 (c). It is worth mentioning that TiO_2 is the main amorphous component of the heterointerfaces and is intentionally deposited in an amorphous structure [31,32].

Amorphous metal-oxide semiconductors, with their visible-light transparency and high bandgap, have tremendous applications in supercapacitors, memristors, and artificial synaptic systems [31,32]. The heterojunction between Au and metal-oxide heterostructures considerably affects the generated charge-storage/trapping phenomenon. A high Schottky barrier at metal/semiconductor heterointerfaces can effectively support and store charge carriers at low voltage for low-energy electronic systems. From another perspective, an ultra-thin crystalline low-resistance electron gate may improve the conductivity of the Au/TiO_2 Schottky junctions. The collected SAED patterns from the heterostructured films show the presence of characteristic rings of crystalline structures, corresponding to the crystalline planes of (112), (222), and (440) of the In_2O_3 ultra-thin film [33]. The high-resolution HR-TEM images depict the sharp heterointerface between the Au and In_2O_3 crystalline film and distinguish the transformation from crystalline In_2O_3 into the adjacent amorphous TiO_2 film (Figure 2c). An EDS analysis was employed to further characterize the chemical composition at the heterointerfaces. Figure 2d depicts the EDS map of the main components of the ALD films. The elemental separation at the heterointerfaces confirms the formation of sharp heterointerfaces. To further investigate the elemental composition, the EDS elemental line scan was employed to demonstrate the distribution of the Au (substrate), In, Ti, Pt (lamella support layer), and O elements at the TiO_2-In_2O_3/Au heterojunctions (Figure 2e). The study on the elemental distribution at the Au, In_2O_3, and TiO_2 heterointerfaces depicts the elemental distinction between the Au (substrate), In_2O_3, and TiO_2 heterojunctions. Partial diffusion of indium and titanium is observed at the TiO_2-In_2O_3 heterointerfaces, with indium and titanium diffusing into each other. Therefore, we employed XPS studies to further investigate the oxidation states of elements at the TiO_2-In_2O_3 heterointerfaces.

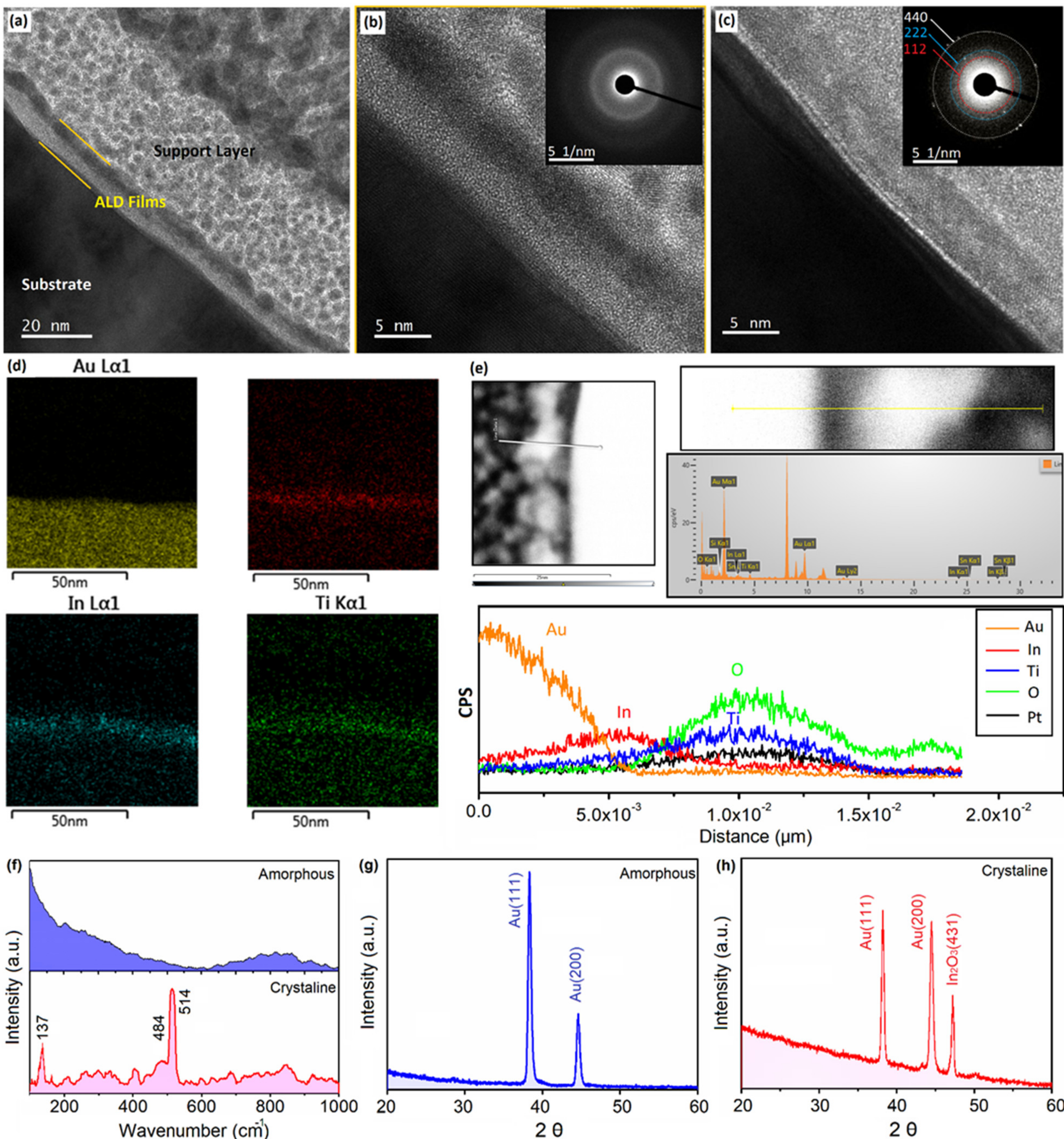

Figure 2. The HR-TEM images and chemical analysis of the heterointerface characteristics: (**a**) The low-magnification and (**b**) high-magnification cross-sectional TEM image and SAED pattern from the TiO_2-In_2O_3 (α) heterointerfaces; (**c**) high-magnification cross-sectional TEM image and SAED pattern from the TiO_2-In_2O_3 (c) heterointerfaces; (**d**) the EDS map elemental analysis accompanied by the (**e**) EDS line elemental analysis of the TiO_2-In_2O_3 heterointerfaces; (**f**) the Raman spectra of In_2O_3 films before and after thermal annealing. (**g**) The XRD pattern of as-deposited amorphous In_2O_3 film. (**h**) The XRD pattern of annealed crystalline In_2O_3 film.

We further investigated the Raman spectra of 5.0 nm In_2O_3 films before and after thermal annealing. The Raman study of the as-deposited film shows a broad spectrum without any distinguished peaks (Figure 2f). The lack of characteristic vibration peaks of In-O bonds in the 5.0 nm thin transparent In_2O_3 films can be attributed to the absence of well-aligned crystalline metal-oxide structures. In contrast, the Raman study of the

annealed In_2O_3 films reveals the presence of characteristic Raman peaks of In-O bonding at the corresponding wavenumbers of 137, 484, and 514 cm^{-1} [34,35]. High-resolution X-ray diffraction (HR-XRD) analysis provides further evidence on the nature of as-deposited and thermally treated In_2O_3 films. The HR-XRD spectra of the 5.0 nm-thick as-deposited In_2O_3 film on an Au substrate (Figure 2g) showed only the characteristic peaks of crystalline Au planes (111) and (200), corresponding to XRD card No. 01-071-3755 [36,37]. In contrast, the XRD measurement of the thermally annealed In_2O_3 film revealed (Figure 2h) a new peak at 47.2°, corresponding to the (431) peak of In_2O_3 (ICPDS #06-0416) [38,39]. These XRD measurements, accompanied by TEM results, confirm the development of crystalline structures in ultra-thin In_2O_3 films after thermal annealing. Therefore, it is expected that the characteristics of the Au/TiO_2 heterointerface are altered by employment of an ultra-thin In_2O_3 electronic gate. Therefore, we investigate the XPS spectra of TiO_2-In_2O_3/Au heterojunctions before and after thermal annealing. Figure A1 represents the surface morphology of In_2O_3 films before and after thermal annealing. According to the AFM measurements, the roughness of In_2O_3 films increased slightly from 450 pm (as-deposited In_2O_3 films) to 860 pm after thermal annealing (Table A1).

The XPS spectra of heterostructured ALD films before and after thermal annealing were investigated and are presented in Figure 3. We measured the XPS spectra of elemental titanium and indium at both the surface (1.0 nm depth) and the TiO_2-In_2O_3 heterointerfaces of the ALD films (5.0 nm depth). Figure 3a shows the In $3d_{5/2}$, In $3d_{3/2}$, Ti $2p_{3/2}$, and Ti $2p_{5/2}$ peaks at 443.6 eV, 451.03 eV, 458.07 eV, and 463.84 eV, respectively. These spectra were collected from the 1.0 nm depth of as-deposited TiO_2-In_2O_3 heterostructured films after the initial Ar milling process. Subsequently, we examined the same sample after further ion milling to reach the TiO_2-In_2O_3 heterointerfaces (Figure 3b). For this purpose, we developed In_2O_3 (5.0 nm)-TiO_2 (5.0 nm) ALD films. When XPS measurements were performed at the heterointerfaces (5 nm), the intensity of the In 3d5/2 and In 3d3/2 peaks increased significantly. However, the Ti $2p_{3/2}$ and Ti $2p_{1/2}$ peaks were deconvoluted into two individual peaks, corresponding to ionic Ti^{3+} and Ti^{4+}. The Ti^{3+} peaks at 456.8 eV and 462.2 eV indicate the presence of titanium sub-oxides [40,41], while the Ti^{4+} peaks at 458.4 eV and 464.1 eV are attributed to TiO_2 [40,41] (Figure 3b). This confirms that the Ti element exists in different oxidation states at the TiO_2-In_2O_3 heterointerfaces. We further analyzed the ratio of valence states of titanium oxide films based on their intensity. The results confirm that the Ti^{3+} valence state of titanium sub-oxides has a considerable presence at the TiO_2-In_2O_3 heterointerfaces (Figure 3b). Additionally, we observed that the VBM values are the same for both amorphous and crystalline In_2O_3 films (Figure 3c). To understand the effect of the crystalline state of the In_2O_3 film on the heterointerface characteristics, XPS studies were performed on TiO_2-In_2O_3 (c) films. Figure 3d,e show the characteristic XPS peaks of Ti 2p and In 3d of the heterostructured films at the surface (1.0 nm depth) and at the heterointerfaces (5.0 nm depth), respectively. Similar to the as-deposited TiO_2-In_2O_3 films, the surface characteristics of the TiO_2-In_2O_3 films clearly show evidence of the Ti^{4+} oxidation state, while the heterointerfaces exhibit the XPS characteristics of both Ti^{3+} and Ti^{4+} (Figure 3d vs. Figure 3e). The presence of structural vacancies in the annealed In_2O_3 film (Figure 1d) can provide favorable conditions for the atomic elemental and vacancy exchange at the vicinity of heterointerfaces. The following measurement of VBM of as-deposited and annealed TiO_2-In_2O_3 heterointerfaces (Figure 3f) confirm the considerable shift of VBM from 1.0 eV to 2.48 eV after thermal annealing of In_2O_3/Au films. This tangible difference between the VBM of TiO_2-In_2O_3 (α) and TiO_2-In_2O_3 (c) heterostructures originates from the developed two-dimensional heterointerfaces between amorphous and crystalline In_2O_3 with the TiO_2 film.

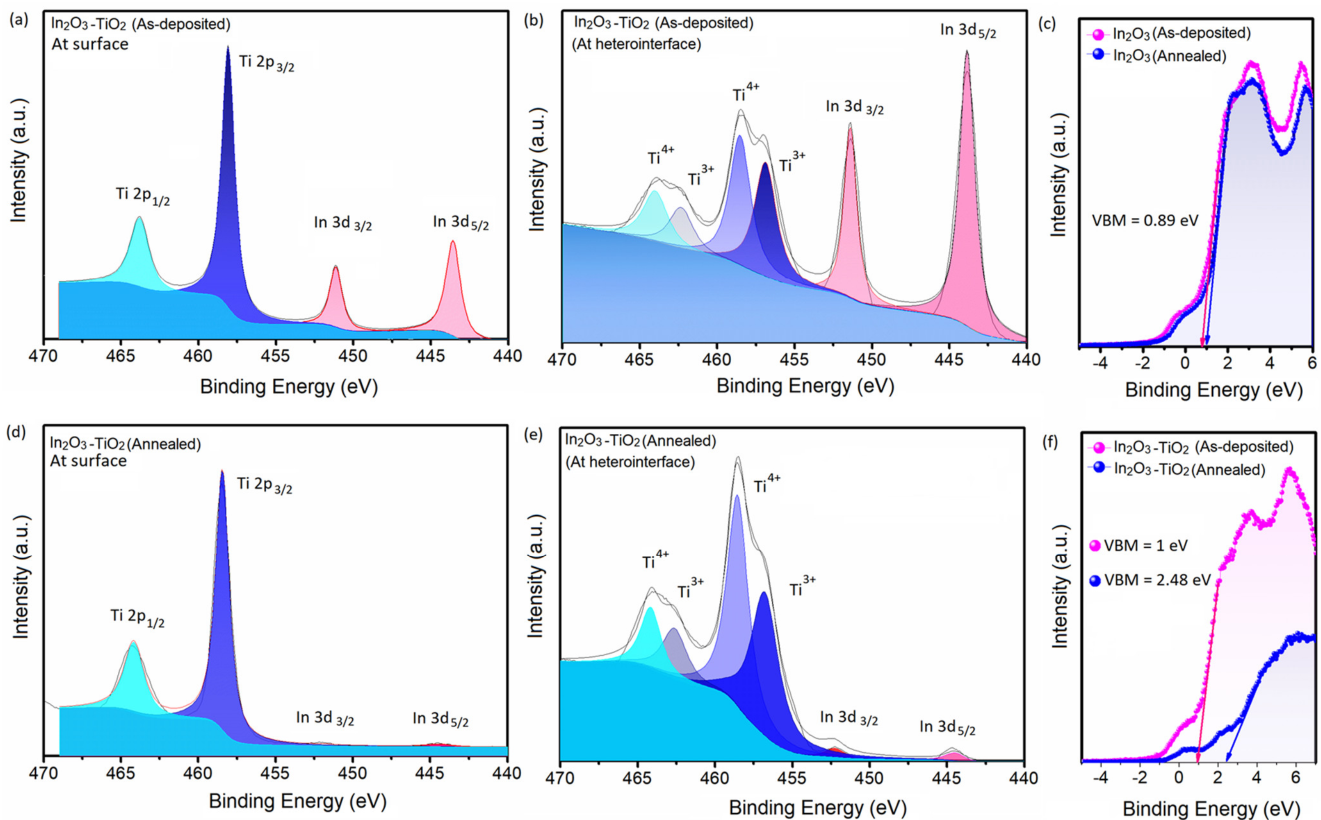

Figure 3. The XPS spectra of Ti 2p and In 3d of as-deposited TiO_2-In_2O_3 (**a**) at surface and at (**b**) heterointerfaces. (**c**) The VBM of as-deposited and amorphous In_2O_3 film. (**d**) The XPS spectra of Ti 2p and In 3d of annealed TiO_2-In_2O_3 films (**d**) at surface and at (**e**) heterointerfaces. (**f**) The VBM of as-deposited and amorphous TiO_2-In_2O_3 film.

3.2. Supercapacitive and Charge-Storage Dynamics

Due to the considerable decrease in the dimensions of nanodevices, conventional methods for characterizing their chemical and electrical properties are neither effective nor precise. Traditional techniques, such as one-dimensional capacitance-voltage (C-V) measurements, do not provide accurate results for observing charge transfer phenomena and supercapacitive characteristics in ultra-thin films and 2D heterointerfaces. To achieve efficient and reliable results, scanning capacitance microscopy (SCM) was employed to image surface characteristics and observe charge transfer mechanisms and electronic phenomena with high spatial resolution [42,43]. SCM falls in the category of scanning probe microscopy (SPM) techniques. The working mechanism of this non-destructive AFM technique is presented in Figure 4a. A typical scanning capacitance microscope specifically monitors variations in spatial capacitance and maps localized charges and electric defects with nanoscale resolution. One of the main applications of SCM is the investigation of charge trapping and detrapping phenomena in ultra-thin metal-oxide layers in two dimensions [44,45]. Consequently, the metal-oxide semiconductor/Au heterojunctions in this study were investigated using SCM.

Figure 4a depicts a typical scheme of the SCM during the evaluation of the charge transfer phenomenon in the AFM tip/TiO_2-In_2O_3/Au heterojunctions. Upon the application of voltage to the Pt-coated AFM tip, a metal-oxide semiconductor (MOS) capacitor-based system is developed. This MOS capacitor is composed of two parallel capacitors in a series. In Figure 4a, the contact point between the probe tip and the sample forms a MOS structure, which can be viewed electrically as a system where the capacitance of the oxide film (C_{ox}) on the semiconductor surface is connected in parallel with the capacitance of the electron channel. The charge transfer phenomenon in the TiO_2-In_2O_3 heterostructured films can

be determined by the carrier depletion/concentration at the heterointerfaces. Considering the polarity of the samples in our setup, the heterostructured film acts as the main oxide layer, and the AFM tip/TiO_2 or the In_2O_3/Au heterointerfaces act as the depletion layers (Figure 4a,b).

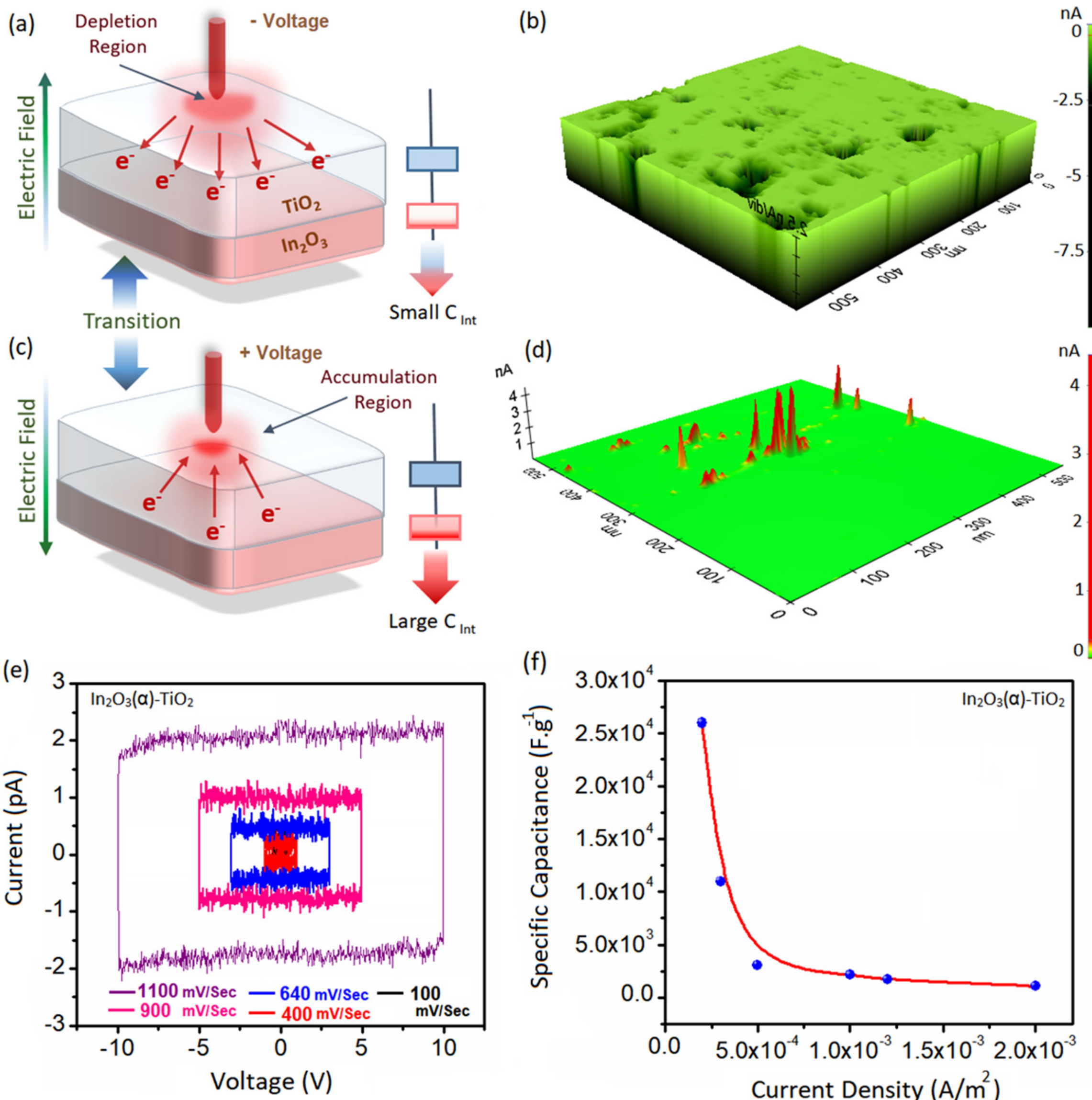

Figure 4. (**a**) The graphical scheme, depicting the charge distribution in heterostructured films when the tip is in negative voltage and (**b**) the corresponding current map of the 500 nm^2 of heterostructured films. (**c**) The graphical scheme, depicting the charge distribution in heterostructured film when the tip is in positive voltage and (**d**) the corresponding current map of the 500 nm^2 of heterostructured films. (**e**) The I-V hysteresis graphs of the AFM tip/TiO_2-In_2O_3 (α)/Au heterojunctions at different applied voltages. (**f**) The variation of specific capacitance of the same heterojunction vs. current density.

When the AFM tip is in the negative voltage state (with Au in the positive voltage state), a depletion layer forms just below the AFM probe, adjacent to the AFM tip/TiO_2 semiconductor heterointerfaces (Figure 4a). The corresponding three-dimensional (3D) current map of the heterostructured semiconductor film is presented in Figure 4b. This current map is measured under a constant AFM tip voltage of −1.0 V. The dark pinholes in the current map indicate the formation of filamentary current channels, initiated from the AFM tip towards the Au substrates through TiO_2-In_2O_3 film. By changing the direction of the electric field, the size of accumulated layers decreases considerably (Figure 4c). In

this state, the largest depletion regions form adjacent to the In_2O_3/Au heterointerfaces. Figure 4d depicts the 3D current map of this system, where the current filaments are ignited, generated, and expanded from the In_2O_3/Au heterointerfaces and then reach the AFM tip (Figure 4c). Here, the capacitance of the In_2O_3/Au heterointerfaces (C_{In}) plays the main role in controlling the charge transfer through the metal/semiconductor heterojunction. When the In_2O_3/Au gate has a low capacitance value (small C_{In}) and the AFM tip is in the negative voltage state, the charge accumulation reaches its minimum level (Figure 4a). However, when the In_2O_3/Au gate has a large capacitance value (large C_{In}) and the AFM tip is in the positive voltage state, the charge accumulation reaches its maximum level (Figure 4c). Therefore, we used the latter conditions to evaluate the charge accumulation state in the AFM Pt tip/TiO_2-In_2O_3 (α)/Au heterojunction. We particularly chose the as-deposited amorphous In_2O_3 (α), which has higher resistance for charge transfer compared to crystalline In_2O_3. Figure 4e shows the results of the I-V curves for the mentioned heterojunctions. The formation of an electrical double layer capacitor (EDLC) is clearly observed in the I-V graph of the AFM Pt tip/TiO_2-In_2O_3 (α)/Au heterojunction. The increase in applied voltage is accompanied by the expansion of the I-V loops, confirming the supercapacitive behavior of the developed heterojunction. The scan rate increased gradually from 100 mV.s in ±1 V measurement range to 1100 mV.s in ±10 V in cyclic measurement range.

Therefore, we conducted a set of experiments to measure the specific capacitance of the developed heterojunction at various current densities (Figure 4f). We measured the current densities based on the developed current filaments between the AFM tip and Au sublayer films, passing through the TiO_2-In_2O_3 heterostructure. It was observed that the specific capacitance of the AFM Pt tip/TiO_2-In_2O_3 (α)/Au heterojunction declined from the maximum value of 2.6×10^4 $F.g^{-1}$ to a constant value of 2.1×10^3 $F.g^{-1}$. We realized that the lower thickness of the TiO_2 film does not necessarily provide higher specific capacitance, but it may increase the power consumption of the devices for possible applications.

We further investigated the I-V cyclic characteristics (Figure 5) and charge transfer mechanism in TiO_2-In_2O_3 heterojunctions. To this aim, we measured the I-V characteristics of In_2O_3 (α), In_2O_3 (c), and TiO_2-In_2O_3 (c) heterojunctions. Here, the thermally annealed In_2O_3 film was employed as the electron gate at the TiO_2-In_2O_3/Au heterojunction. The phase transformation from the amorphous to crystalline state alters the mechanism of charge transfer [46,47]. As discussed in the previous section, localization is expected to be the main mechanism of charge transfer in amorphous In_2O_3 films. Upon the structural transition from the amorphous to the crystalline state, the charge transfer mechanism changes from localization to hopping, multi-phase percolation, scattering, and ultimately to bulk conductivity in the fully crystalline In_2O_3 (c) structure. Therefore, we employed conductive atomic force microscopy (c-AFM) to monitor charge transfer at the AFM Pt tip/TiO_2-In_2O_3 (c)/Au heterojunction.

Figure 5a shows the cyclic I-V curves of c-AFM Pt tip/In_2O_3 (α)/Au heterojunction at 1st, 20th, and 100th cycles of measurements. The current level in the positive applied voltage does not change considerably, while a gradual increase in current was observed at negative applied voltage. This difference can be attributed to the characteristics of Pt/In_2O_3 and In_2O_3/Au heterojunctions. When the positive voltage is applied at the c-AFM tip, the electron accumulation layer is formed at c-AFM Pt tip/In_2O_3 (α) heterointerfaces, while the electron depletion region is formed at the Pt tip/In_2O_3 (α) heterointerfaces at negative applied voltage. The following measurements of heterointerface resistance of the c-AFM Pt tip/In_2O_3 (α)/Au heterojunction showed the gradual decrease in heterojunction resistance by the increase in cycles of measurements (Figure 5b). The observed decrease in heterojunction resistance can be attributed to the gradual formation and the size expansion of conductive channels in amorphous In_2O_3 (α) film. We further investigate the I-V characteristics of crystalline In_2O_3 (c) at two different ranges of voltages of ±1 V and ±10 V (Figure 5c,d). The considerable increase in current level from pA in In_2O_3 (α) to nA scales in In_2O_3 (c) can be related to the improved level of conductance in crystalline films

compared with that of amorphous films. This is particularly meaningful when the level of currents increased to hundreds of nA when the applied voltage increased from ±1V to ±10 V during cyclic I-V measurements (Figure 5c,d). This confirms that the applied voltage has direct impact on the increase in level of conductivity of heterojunctions.

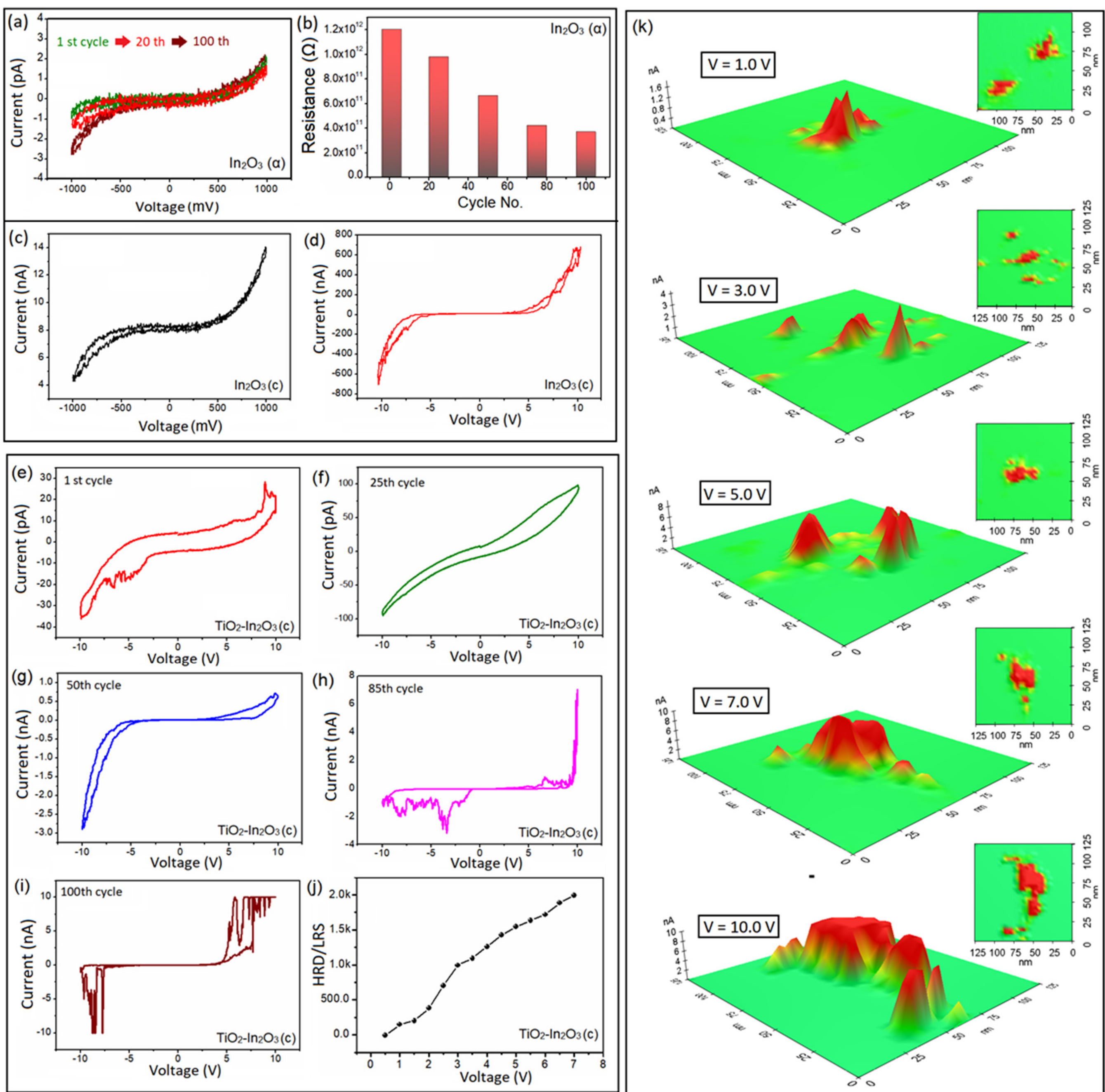

Figure 5. (**a**) The I-V cyclic curves of c-AFM Pt-coated tip/In_2O_3 (α)/Au heterojunctions. (**b**) The variation of contact resistance of c-AFM Pt tip/In_2O_3 (α)/Au heterojunctions at various I-V cyclic measurements. (**c**) The cyclic 1st I-V curve of In_2O_3 (**d**) within ±1 V and (**f**) ±10 V. (**e**–**i**) The I-V hysteresis of the TiO_2-In_2O_3 (c) gate at various cycles, depicting the transformation from non-zero I-V hysteresis in nanobatteries (1st and 25th cycles) to pseudocapacitors (50th cycle) and finally memristors (85th and 100th cycles). (**j**) The variation of HRS to LRS ratio vs. the applied voltage. (**k**) The 3D current map the TiO_2-In_2O_3 (c) heterostructured thin film, investigated at various constant applied voltages.

Figure 5e–i shows the typical cyclic I-V curves of the c-AFM Pt-coated tip/ TiO_2-In_2O_3 (c)/Au heterojunction at various cycle measurements. The measurements were performed inside an enclosed chamber, under the flow of Ar inert gas to prevent the undesired reaction of the atmospheric humidity with surface of metal-oxide semiconductors during the c-AFM measurements. The initial cycles of the I-V curve for this heterojunction displays a non-zero I-V hysteresis (Figure 5e), which is similar to the faradic pseudocapacitance behavior of ultra-thin metal-oxide films [14,48]. As the cycles progress, there is a transformation from faradic pseudocapacitance (Cycles 1 and 25 in Figure 5e,f) to nanobattery-like capacitance (Cycle 50, Figure 5g) and eventually to resistive switching memristive behavior (Cycles 85 and 100 in Figure 5h,i). Correspondingly, the current level increases from 20 pA in the first cycle to 10 nA in the 100th cycle. We further investigate the effect of applied voltage on the current levels in high-resistance state (HRS) and low-resistance state (LRS) of the TiO_2-In_2O_3 (c)-based memristor. The variation of HRS to LRS ratio vs. the applied voltages for c-AFM Pt tip/TiO_2-In_2O_3 (c)/Au heterojunctions is presented in Figure 5j. The increase in applied voltage was accompanied by the gradual increase in HRS to LRS ratio. The highest HRS to LRS ratio of 2.0 k was measured when the compliance current of the device was set at 10.0 nA (Figure 5j). Compared with the supercapacitive characteristics of TiO_2-In_2O_3 (α) heterojunctions, the TiO_2-In_2O_3 (c) heterointerfaces showed the gradual changes of charge-storage and transfer mechanisms. The gradual shift of the non-zero I-V curves (pseudocapacitors) into memristors depicts the change of mechanism of charge transfer at heterointerfaces. The phenomenon of "non-zero crossing I-V hysteresis curves" arises from various factors, including the polarization of ferroelectric or piezoelectric domains, the involvement of additional capacitance effects, and the formation of nanobatteries within the heterojunctions during the cyclic I-V measurements [49,50]. As the number of I-V cycles increases, the shapes of the I-V graphs change. The generation of an electromotive force in heterojunctions is accompanied by redox reactions at the heterointerfaces. This internal driving force, which resembles a nanobattery, generates additional internal current within the system, resulting in the observation of non-zero I-V curves. This electrical behavior is physically similar to the characteristics of metal-oxide memristor materials coupled with a pseudocapacitor or a nanogenerator battery [32,40]. As the number of cycles increases, the stored charges in the TiO_2-In_2O_3 (c)/Au heterointerface increase until there is a full transition from non-zero to zero-crossing I-V cyclic behavior (Cycle 75). The subsequent I-V cyclic behavior of the heterojunctions is similar to the performance of a memristor device. This behavior appears to occur due to the accumulation and storage of charge carriers in the TiO_2-In_2O_3 (c) heterojunctions or at the electron channels at the metal/semiconductor heterointerfaces. Therefore, we observed that the structure of the In_2O_3 gate film directly alters the charge-storage mechanism in TiO_2-In_2O_3/Au heterojunctions.

Figure 5k presents the 3D current maps of the AFM Pt-coated tip/TiO_2-In_2O_3 (c)/Au heterojunction at various applied voltages on c-AFM Pt-coated tip: 1.0, 3.0, 5.0, 7.0, and 10.0 volts. In each measurement, the applied voltage on the c-AFM tip was constant. It is observed that the gradual increase in applied voltage is accompanied by an increase in the filamentary current formed between the Au sublayer and the c-AFM probe tip. The filamentary current increased from 250 pA at an applied voltage of 1.0 V to a few nA at an applied voltage of 7.0 V. Increasing the applied voltage to 10.0 V resulted in a filamentary current exceeding 10 nA, which is the measurement threshold of the AFM device (Figure 5k). Additionally, it was observed that the increase in applied voltage was accompanied by an increase in the size and dimension of the filamentary currents. In detail, the conductive atomic force microscopy (c-AFM) analysis provides information on the filamentary currents formed during measurements. These currents are collected for image analysis, where specialized software measures the average diameter of the filamentary currents. The graphical indices in Figure 5k depict this gradual alteration in the dimensions of the filamentary currents. A typical filamentary current has an average diameter of 20.0 nm at an applied voltage of 1.0 V. With an increase in applied voltage, the diameter of a filamentary current increases significantly. A typical diameter of a filamentary current is

50.0 nm at an applied voltage of 7.0 V and finally reaches 75.0 nm at an applied voltage of 10.0 V (Figure 5k). At this stage, the dielectric layer is almost broken and can no longer function as a charge-storage or capacitor layer. Figure A2 (Appendix A) graphically depicts the magnitude and size of the filamentary currents expanded in TiO_2-In_2O_3 ultra-thin films during the c-AFM measurements. The results clearly show that the filamentary currents are formed, expanded, and deteriorated in the heterostructured oxide films. From an applied voltage of 1.0 V to 7.0 V, the current magnitude increases from a few hundred pA to several nA.

Figure 6 schematically illustrates the mechanism of charge storage and transfer at the c-AFM Pt tip/TiO_2-In_2O_3 (c)/Au heterointerfaces after thermal equilibrium. The work functions of Pt and Au conductive channels are assumed to be 5.1~5.9 eV and 5.1~5.4 eV, respectively. UV–Vis measurements confirmed that the bandgaps of In_2O_3 (c) and TiO_2 are 1.97 eV and 3.3 eV, respectively (Figure A3). The ΔE_c and ΔE_v at the TiO_2-In_2O_3 (c) interface are 3.89 eV and 2.2 eV, respectively, as detailed in Appendix B and Figure A4. Figure 6a shows the energy band alignment of the c-AFM Pt-coated tip/TiO_2-In_2O_3 (c)/Au heterojunction under zero applied voltage. Charge trap centers in the TiO_2 film are located 0.2 eV below the conduction band of TiO_2 [51–53]. Given the ΔE_c of 2.2 eV at the TiO_2-In_2O_3 (c) interface, the Ti-associated trap energy levels are 2.0 eV above the conduction band of the In_2O_3 (c) film. The polarization of In_2O_3 (c)/Au has considerable impact on the charge-storage dynamics at heterointerfaces. Considering the Schottky barrier height at the interfaces between the Au and Pt electrodes with the TiO_2 semiconductor, it is plausible that carrier trapping in the TiO_2 film primarily occurs through the exchange of electrons with the Pt electrode under forward bias voltage. However, the presence of a significant number of trapping sites at the Au/In_2O_3(c) interface determines the resistance value and the switching mechanism of the memristor. Figure 6b depicts the occupation of Ti trapping sites in the TiO_2 film via transmitted electrons from the Pt electrode under forward bias voltage. Once the trapping sites in the TiO_2 films are saturated, charge carriers are transmitted into the In_2O_3 (c)/Au interface. Upon applying a higher voltage, the set process is completed, and the device remains in the low-resistance state (LRS) (Figure 6b,c).

In reverse bias voltage, the barrier height between the In_2O_3 (c)/Au interface and the TiO_2 amorphous film is too high (~1.97 eV); thus, the current flow under the applied bias voltage occurs through the tunneling and thermionic emission (Figure 6d). By applying a positive reversed bias voltage on the Au electrode, the voltaic generated charge carriers try to pass the high-height Schottky barrier between In_2O_3 (c)/Au and amorphous TiO_2 heterointerfaces (Figure 6e). This process can be longer and altered based on the operating bias voltage and the amount of injected and stored charges in both heterointerfaces and TiO_2 film. Considering the higher thickness of the TiO_2 film (19.0 nm) compared to the In_2O_3 film (5.0 nm), both Fowler–Nordheim (F–N) [54–56] and direct tunneling mechanisms [57–60] are likely responsible for charge transfer (Figure 6e). In LRS state, the high-height Schottky barrier induces high-barrier and extended storage capacity, i.e., the injection of electrons from In_2O_3 (c)/Au into amorphous TiO_2 film is inconsiderable. However, once the stronger reverse voltage is applied on Au electrodes, or positive voltage on Pt electrodes, the Fermi level of In_2O_3 (c)/Au heterostructure is pulled up above the trap levels in TiO_2 film, and then it facilitates the restoration of the HRS state (Figure 6e). When In_2O_3 (c)/Au is at upward polarization, the electron accumulation occurs at In_2O_3 (c)/Au heterointerfaces. In the downward polarization, the location of ionized oxygen vacancies are localized. It causes a separation between the ionized oxygen vacancies and plasmonically generated electrons that finally inhibit the recombination reactions (Figure 6e). The electron accumulation at In_2O_3 (c)/Au heterointerfaces enables the electron/holes recombination at heterointerfaces, where $V_0^{2+} + 2e^- \rightarrow V_0$.

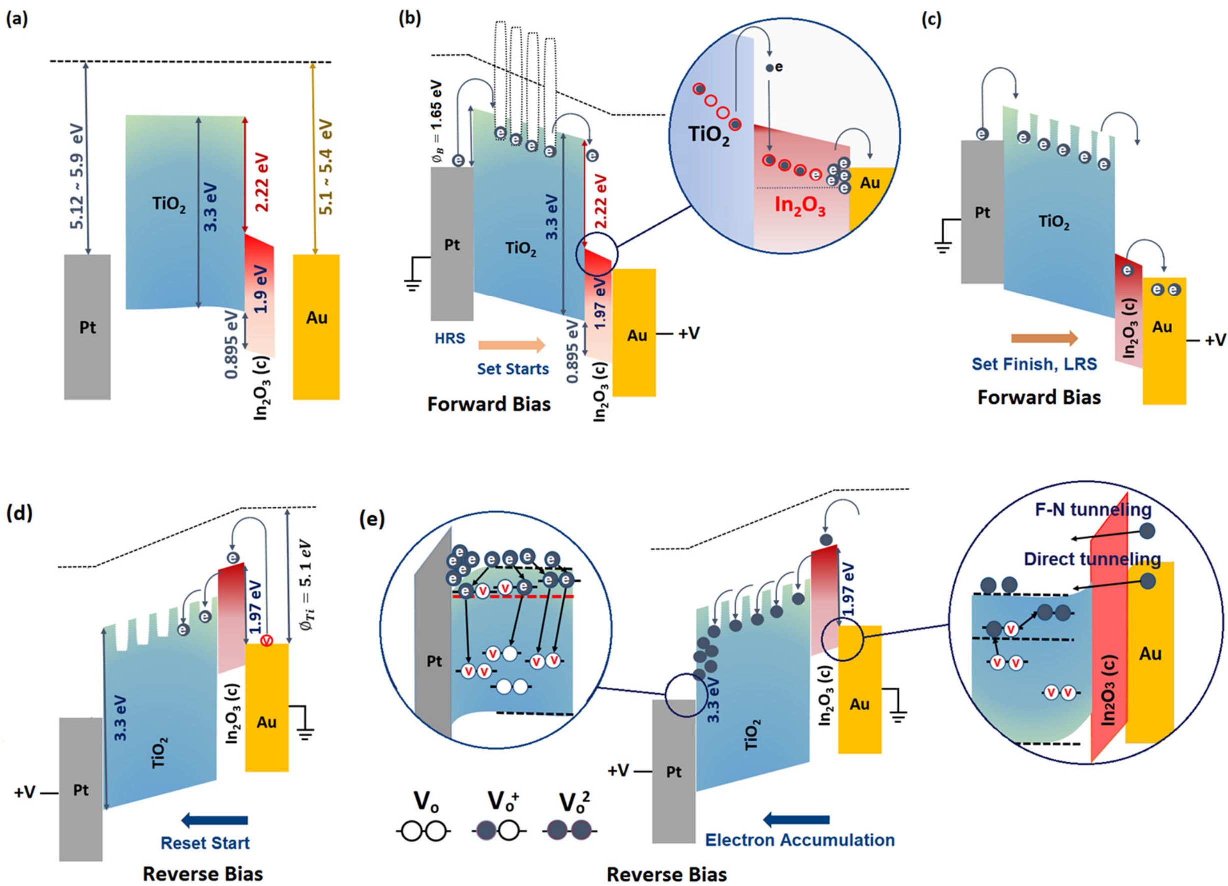

Figure 6. (**a**) The schematic of energy band alignment diagram of the Pt/TiO_2-In_2O_3 (c)/Au heterojunction at 0.0 applied voltage. (**b**) The illustration of charge trapping and detrapping process when a positive bias voltage is applied on an Au electrode. The trapped electrons are released and transmitted to Au electrodes, and (**c**) LRS is achieved. (**d**) The schematic of energy band alignment at Pt/TiO_2-In_2O_3 (c)/Au heterojunctions when the positive voltage is applied on Pt electrode and (**e**) the corresponding mechanisms of charge transfer at In_2O_3 (c)/Au and Pt/TiO_2 heterointerfaces.

4. Conclusions

Understanding the mechanism of charge transport at ultra-thin metal-oxide semiconductor hybrid interfaces provides fundamental information for the design and fabrication of functional tunable nanoelectronic channels. This study focuses on the design, characterization, and evaluation of capacitive-coupled memristive behavior in ALD-developed ultra-thin TiO_2-In_2O_3/Au heterojunctions. The structure of the ultra-thin In_2O_3 film (5.0 nm) directly impacts the charge transfer mechanism at In_2O_3/Au heterointerfaces. An as-deposited amorphous In_2O_3 film provides the 2D hybrid interfaces with supercapacitive characteristics. The TiO_2-In_2O_3 (α)/Au heterojunctions with an amorphous indium oxide electron channel exhibited a maximum specific capacitance of 2.6×10^4 F.g^{-1}. The supercapacitive behavior of these heterointerfaces altered considerably after thermal annealing of the In_2O_3 film. Using a crystalline In_2O_3 (c) film as the gate electrode at TiO_2-In_2O_3 (c)/Au heterointerfaces significantly changed the dynamics of charge transfer at these electronic heterojunctions. The transformation of the charge transfer mechanism was accompanied by a shift in the electronic gate's behavior from supercapacitive to nanobattery-like and then to pseudocapacitive performance. Finally, memristive behavior was observed after sequential cyclic I-V hysteresis measurements. Therefore, the tunable modification of electronic characteristics of In_2O_3 (c)/Au heterointerfaces through thermal annealing enables the design of hybrid nanoelectronic devices with supercapacitive-coupled memristive functionalities.

Author Contributions: M.K.A. introduced the idea; designed the study; and performed atomic layer deposition, materials characterization, fabrication, and evaluation of micro-electronic devices. M.K.A., N.S.L. and S.Z. discussed and analyzed the results. M.K.A. wrote the paper. S.Z. supervised the study. All authors have read and agreed to the published version of the manuscript.

Funding: The work was supported by the Research & Development Program of the Ghent University Global Campus, South Korea.

Institutional Review Board Statement: Not applicable.

Informed Consent Statement: Not applicable.

Data Availability Statement: The raw data supporting the conclusions of this article will be made available by the authors on request.

Acknowledgments: During the preparation of this work, the authors used Chat GPT in order to check the grammar and spelling. After using this tool, the authors reviewed and edited the content as needed and take full responsibility for the content of the publication.

Conflicts of Interest: The authors declare no conflicts of interest.

Appendix A

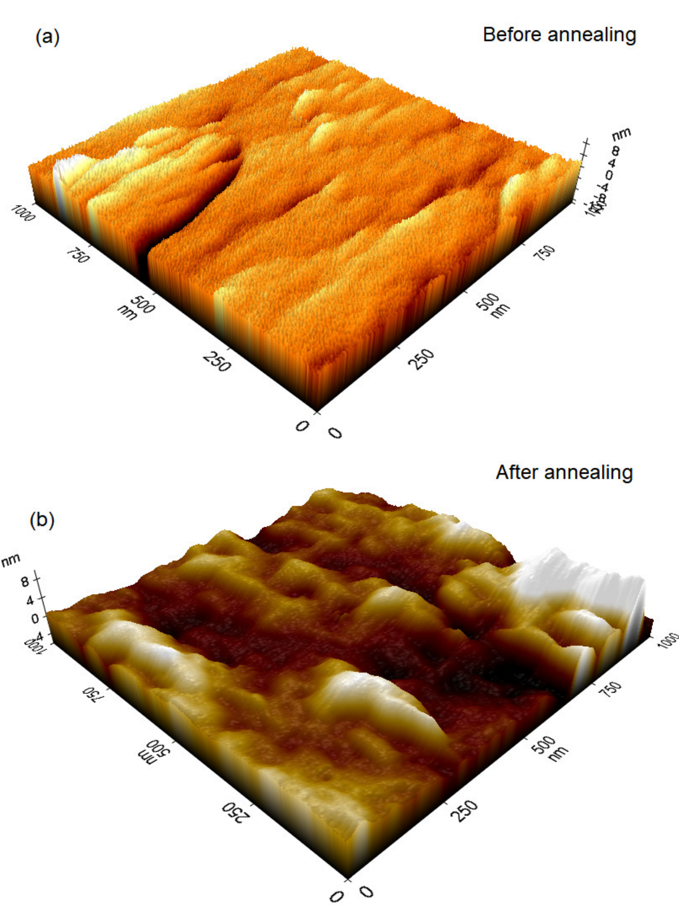

Figure A1. The 3D AFM surface morphology of In_2O_3 films (**a**) before and (**b**) after thermal annealing.

Table A1. AFM data for as-deposited and annealed In_2O_3 films.

Sample	Measured Area	Roughness
In_2O_3 (as-deposited)	1 μm^2	450 pm
In_2O_3 (annealed)	1 μm^2	860 pm

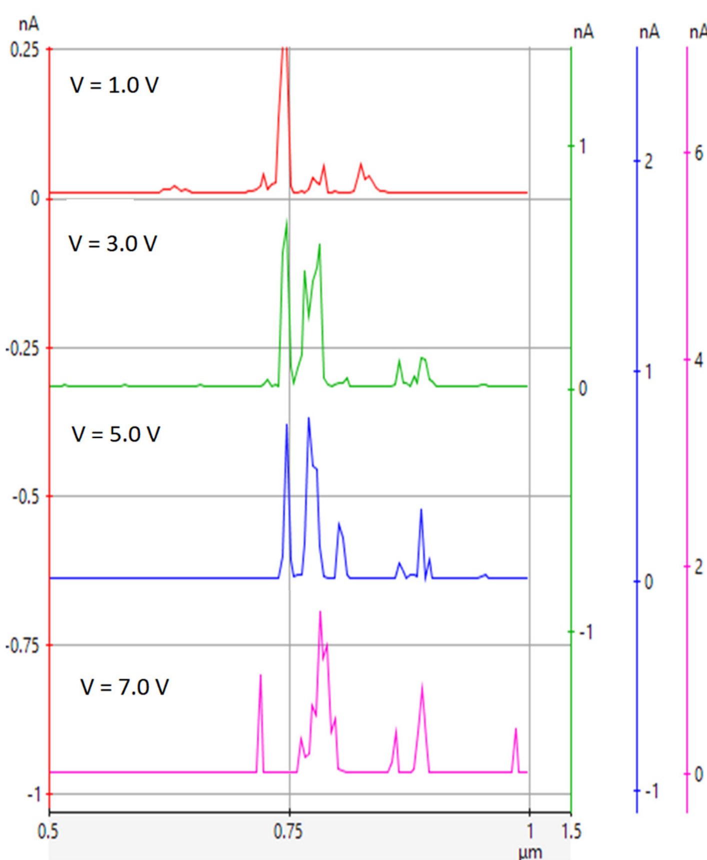

Figure A2. The corresponding line profile of the filamentary currents formed in the heterostructured oxide during the generation of current map of surface.

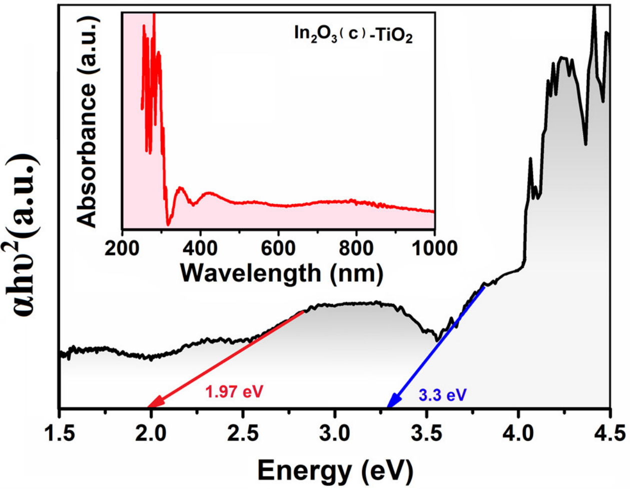

Figure A3. The UV–Vis spectra and bandgap of TiO_2-In_2O_3 (c) heterostructure.

Appendix B. Calculation of Energy Band Alignment at Semiconductor Heterointerfaces

Based on Kraut's method, the valence band offset (VBO) can be extracted by following Formula (A1) [48,49]:

$$\Delta E_V = \left(E_{Ti2P}^{TiO_2} - E_{VBM}^{TiO_2}\right) - \left(E_{In3d}^{In_2O_3} - E_{VBM}^{In_2O_3}\right) - \left(E_{Ti2P}^{TiO_2} - E_{In3d}^{In_2O_3}\right) \quad \text{(A1)}$$

where $E_{In3d}^{In_2O_3}$ is core level (CL) spectra of In 3d, $E_{VBM}^{In_2O_3}$ is the valence band maximum (VBM) of In_2O_3 (c), $E_{Ti2P}^{TiO_2}$ is the CL of Ti 2P spectra, and $E_{VBM}^{TiO_2}$ is the VBM of TiO_2. To calculate the

VBM, the XPS spectra of In_2O_3 (c) and TiO_2 were used. To describe the integrated band offsets of the TiO_2-In_2O_3 heterojunction, the corresponding energy difference between conduction bands can be calculated from Formula (A2):

$$\Delta E_C = E_{Bandgap}^{TiO_2} - E_{Bandgap}^{In_2O_3} - \Delta E_V \quad \text{(A2)}$$

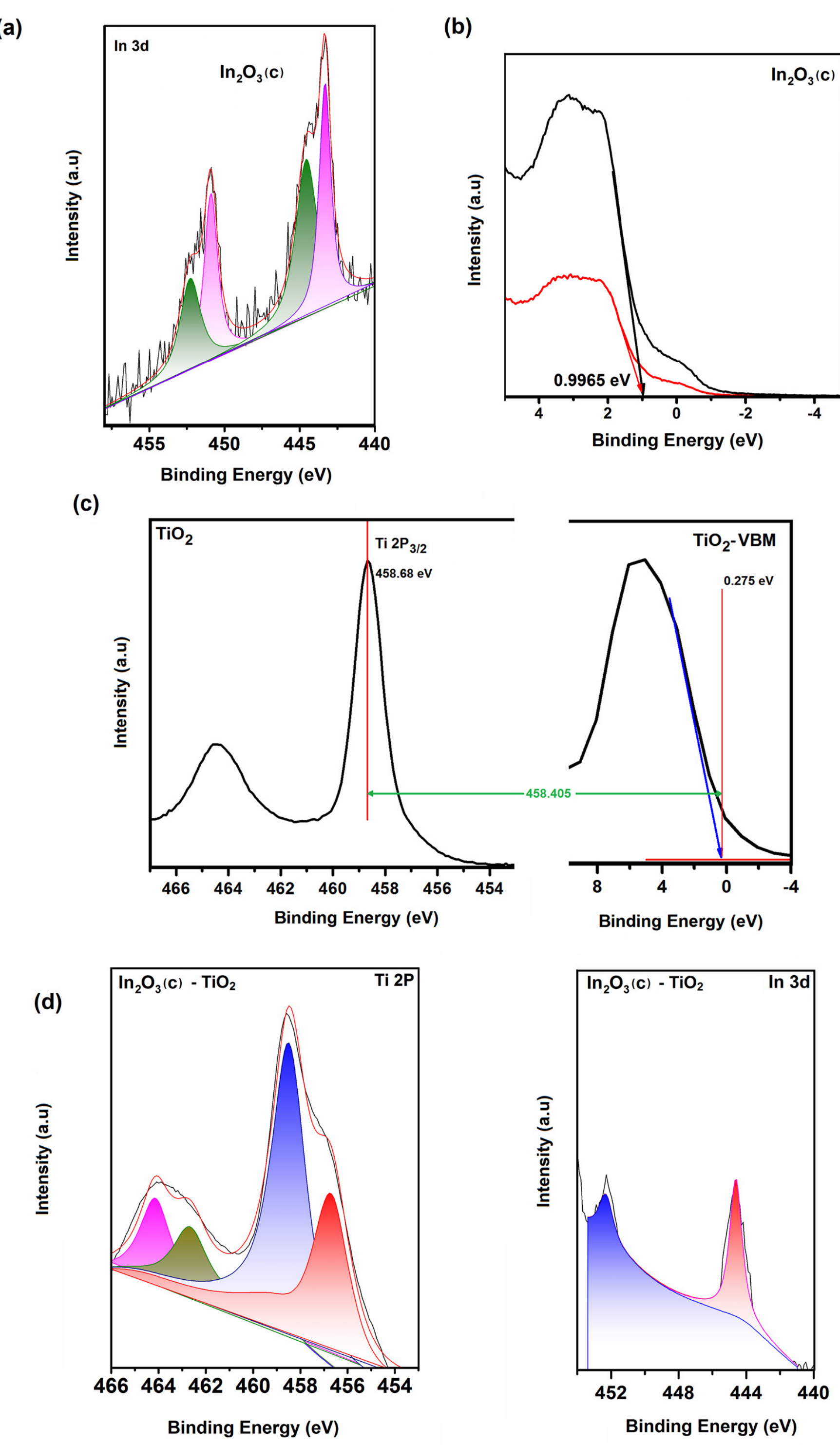

Figure A4. XPS peak parameters for calculation of energy band alignment at In_2O_3 (c)-TiO_2 heterostructure. (**a**) The In3d of In_2O_3 (c), (**b**) VBM of In_2O_3 (c) and In_2O_3 (α), (**c**) The XPS characteristics of TiO_2. (**d**) The Ti2p and In3d peaks of In_2O_3 (c)-TiO_2 heterostructure.

References

1. Zhuiykov, S.; Xu, H.; Karbalaei Akbari, M.; Kumar, S.; Verpoort, F. Atomic layer deposition–state-of-the-art approach to nanoscale hetero-interfacial engineering of chemical sensors electrodes: A review. *Sens. Actuators B Chem.* **2021**, *331*, 129403.
2. Hai, Z.; Karbalaei Akbari, M.; Wei, Z.; Xue, C.; Xu, H.; Hu, J.; Hyde, L.; Zhuiykov, S. TiO_2 nanoparticles-functionalized two-dimensional WO_3 for high-performance supercapacitors developed by facile two-step ALD process. *Mater. Today Commun.* **2017**, *12*, 56–62.
3. Xu, H.; Karbalaei Akbari, M.; Zhuiykov, S. 2D semiconductor nanomaterials and heterostructures: Controlled synthesis and functional applications. *Nanoscale Res. Lett.* **2021**, *16*, 94. [CrossRef] [PubMed]
4. Xu, H.; Karbalaei Akbari, M.; Hai, Z.; Wei, Z.; Hyde, L.; Verpoort, F.; Xue, C.; Zhuiykov, S. Ultra-thin MoO_3 film goes wafer-scaled nano-architectonics by atomic layer deposition. *Mat. Des.* **2018**, *149*, 135–144. [CrossRef]
5. Shen, C.; Yin, Z.; Collins, F.; Pinna, N. Atomic layer deposition of metal oxides and chalcogenides for high performance transistors. *Adv. Sci.* **2022**, *9*, 2104599. [CrossRef] [PubMed]
6. Rafailov, P.; Mehandzhiev, V.; Sveshtarov, P.; Blagoev, B.; Terziyska, P.; Avramova, I.; Kirilov, K.; Ranguelov, B.; Avdeev, G.; Petrov, S.; et al. Atomic Layer Deposition Growth and Characterization of Al_2O_3 Layers on Cu-Supported CVD Graphene. *Coatings* **2024**, *14*, 662. [CrossRef]
7. Drnovšek, A.; Kukuruzovič, D.; Terek, P.; Miletić, A.; Čekada, M.; Panjan, M.; Panjan, P. Microstructural, Mechanical and Oxidation Resistance of Nanolayer Sputter-Deposited CrAlN Hard Coatings. *Coatings* **2023**, *13*, 2096. [CrossRef]
8. Karbalaei Akbari, M.; Siraj Lopa, N.; Zhuiykov, S. Atomic Layer Deposition of Ultra-Thin Crystalline Electron Channels for Heterointerface Polarization at Two-Dimensional Metal-Semiconductor Heterojunctions. *Coatings* **2023**, *13*, 1041. [CrossRef]
9. Xu, H.; Karbalaei Akbari, M.; Verpoort, F.; Zhuiykov, S. Nano-engineering and functionalization of hybrid Au–Me_xO_y–TiO_2 (Me = W, Ga) hetero-interfaces for optoelectronic receptors and nociceptors. *Nanoscale* **2020**, *12*, 20177–20188. [CrossRef]
10. Goul, R.; Marshall, A.; Seacat, S.; Peelaers, H.; Hernandez, F.C.R.; Wu, J.Z. Atomic-scale tuning of ultrathin memristors. *Commun. Phys.* **2022**, *5*, 260. [CrossRef]
11. Serb, A.; Bill, J.; Khiat, A.; Berdan, R.; Legenstein, R.; Prodromakis, T. Seamlessly fused digital-analogue reconfigurable computing using memristors. *Nat. Commun.* **2017**, *7*, 12611. [CrossRef] [PubMed]
12. Asif, M.; Kumar, A. Resistive switching in emerging materials and their characteristics for neuromorphic computing. *Mater. Today Electron.* **2022**, *1*, 10004. [CrossRef]
13. Karbalaei Akbari, M.; Hu, J.; Verpoort, F.; Lu, H.; Zhuiykov, S. Nanoscale all-oxide-heterostructured bio-inspired optoresponsive nociceptor. *Nano-Micro Lett.* **2020**, *12*, 83. [CrossRef] [PubMed]
14. Valov, I.; Linn, E.; Tappertzhofen, S.; Schmelzer, S.; van den Hurk, J.; Lentz, F.; Waser, R. Nanobatteries in redox-based resistive switches require extension of memristor theory. *Nat. Commun.* **2013**, *4*, 1771. [CrossRef] [PubMed]
15. Lopa, N.S.; Karbalaei Akbari, M.; Lu, H.L.; Zhuiykov, S. ALD-enabled WO_3-MoO_3 nanohybrid heterostructure for high-performance electrochemical supercapacitors. *J. Energy Storage* **2024**, *84*, 110777. [CrossRef]
16. Salonikidou, B.; Yasunori, T.; Le Borgne, B.; England, J.; Shizuo, T.; Sporea, R.A. Toward fully printed memristive elements: A-TiO_2 electronic synapse from functionalized nanoparticle ink. *ACS Appl. Electron. Mater.* **2019**, *1*, 2692–2700. [CrossRef]
17. Kim, B.; Mahata, C.; Ryu, H.; Ismail, M.; Yang, B.-D.; Kim, S. Alloyed High-k-Based Resistive Switching Memory in Contact Hole Structures. *Coatings* **2021**, *11*, 451. [CrossRef]
18. Cho, H.; Kim, S. Enhancing Short-Term Plasticity by Inserting a Thin TiO_2 Layer in WO_x-Based Resistive Switching Memory. *Coatings* **2020**, *10*, 908. [CrossRef]
19. Hopkin, M. Found: The missing circuit element. *Nature* **2008**, *24*, 789. [CrossRef]
20. Qingjiang, L.; Khiat, A.; Salaoru, I.; Papavassiliou, C.; Hui, X.; Prodromakis, T. Memory impedance in TiO_2 based metal-insulator-metal devices. *Sci. Rep.* **2014**, *4*, 4522. [CrossRef]
21. AlGhamdi, W.S.; Fakieh, A.; Faber, H.; Lin, Y.-H.; Lin, W.-Z.; Lu, P.-Y.; Liu, C.-H.; Salama, K.N.; Anthopoulos, T.D. Impact of layer thickness on the operating characteristics of In_2O_3/ZnO heterojunction thin-film transistors. *Appl. Phys. Lett.* **2022**, *121*, 233503. [CrossRef]
22. Aparna, C.; Mahesha, M.G.; Shetty, P.K. Structural and optical properties of indium oxide thin films synthesized at different deposition parameters by spray pyrolysis. *Mater. Today Proc.* **2022**, *55*, 141–147. [CrossRef]
23. Ramachandran, R.K.; Dendooven, J.; Poelman, H.; Detavernier, C. Low temperature atomic layer deposition of crystalline In_2O_3 films. *J. Phys. Chem. C* **2015**, *119*, 11786–11791. [CrossRef]
24. Buchholz, D.B.; Ma, Q.; Alducin, D.; Ponce, A.; Jose-Yacaman, M.; Khana, R.; Medvedeva, J.E.; Chang, R.P.H. The structure and properties of amorphous indium oxide. *Chem. Mater.* **2014**, *26*, 5401–5411. [CrossRef] [PubMed]
25. Bellingham, J.R.; Phillips, W.A.; Adkins, C.J. Amorphous indium oxide. *Thin Solid Films* **1991**, *195*, 23–32. [CrossRef]
26. Charnas, A.; Zhang, Z.; Lin, Z.; Zheng, D.; Zhang, J.; Si, M.; Ye, P.D. Extremely thin amorphous indium oxide transistors. *Adv. Mater.* **2024**, *36*, 2304044. [CrossRef] [PubMed]
27. Hoch, L.B.; Wood, T.E.; O'Brien, P.G.; Liao, K.; Reyes, L.M.; Mims, C.A.; Ozin, G.A. The rational design of a single-component photocatalyst for gas-phase CO_2 reduction using both UV and visible light. *Adv. Sci.* **2014**, *1*, 1400013. [CrossRef] [PubMed]
28. Shan, F.; Sun, H.; Lee, J.; Pyo, S.; Kim, S. Improved high-performance solution processed In_2O_3 thin film transistor fabricated by femtosecond laser pre-annealing process. *IEEE Access* **2021**, *9*, 44453–44462. [CrossRef]

29. Juodkazis, K.; Juodkazyt, J.; Jasulaitien, V.; Lukinskas, A.; Šebeka, B. XPS studies on the gold oxide surface layer formation. *Electrochem. Commun.* **2000**, *2*, 503–507. [CrossRef]
30. Monopoli, A.; Afzal, A.; Di Francoc, C.; Ditaranto, N.; Cioffi, N.; Nacci, A.; Cotugno, P.; Torsi, L. Design of novel indium oxide supported gold nanocatalysts and their application in homocoupling of arylboronic acids. *J. Mol. Catal. A Chem.* **2014**, *386*, 101–107. [CrossRef]
31. Jeong, H.Y.; Lee, J.Y.; Choi, S.Y. Interface-engineered amorphous TiO_2 based resistive memory devices. *Adv. Funct. Mater.* **2010**, *20*, 3912–3917. [CrossRef]
32. Miyake, R.; Nagata, Z.; Adachi, K.; Hayashi, Y.; Tohei, T.; Sakai, A. Versatile functionality of four-terminal TiO_{2-x} memristive devices as artificial synapses for neuromorphic computing. *ACS Appl. Electron. Mater.* **2022**, *4*, 2326–2336. [CrossRef]
33. Mansiri, S.; Laokul, P.; Klinkaewnarong, J.; Phokha, S.; Promarak, V.; Seraphin, S. Indium oxide (In_2O_3) nanoparticles using Aloevera plant extract: Synthesis and optical properties. *Optoelectron. Adv. Mat.* **2008**, *2*, 161–165.
34. Reyes-Gil, K.R.; Reyes-Garcia, E.A.; Raftery, D. Nitrogen-doped In_2O_3 thin film electrodes for photocatalytic water splitting. *J. Phys. Chem. C* **2007**, *111*, 14579–14588. [CrossRef]
35. Wu, K.R.; Yeh, C.W.; Hung, C.H.; Cheng, L.H.; Chung, C.Y. Photoelectrochemical properties of nitrogen-doped indium tin oxide thin films prepared by reactive DC magnetron sputtering. *Thin Solid Films* **2009**, *518*, 1581–1584. [CrossRef]
36. Ogundare, O.D.; Akinribide, O.J.; Adetunji, A.R.; Adeoye, M.O.; Olubambi, P.A. Crystallite size determination of thermally deposited Gold Nanoparticles. *Procedia Manuf.* **2019**, *30*, 173–179. [CrossRef]
37. Holder, C.F.; Schaak, R.E. Tutorial on powder X-ray diffraction for characterizing nanoscale materials. *ACS Nano* **2019**, *13*, 7359–7365. [CrossRef]
38. Bouhdjer, A.; Saidi, H.; Attaf, A.; Aida, M.S.; JlassI, M.; Bouhaf, I.; Benkhetta, Y.; Bendjedidi, H. Structural, morphological, optical, and electrical properties of In_2O_3 nanostructured thin films. *Optik.* **2016**, *127*, 7319–7325. [CrossRef]
39. Yaragani, V.; Kamatam, H.P.; Deva Arun Kumar, K.; Mele, P.; Christy, A.J.; Gunavathy, K.V.; Alomairy, S.; Al-Buriahi, M.S. Structural, Magnetic and Gas Sensing Activity of Pure and Cr Doped In_2O_3 Thin Films Grown by Pulsed Laser Deposition. *Coatings* **2021**, *11*, 588. [CrossRef]
40. Biesinger, M.C.; Lau, L.W.M.; Gerson, A.; Smart, R.S.C. Resolving surface chemical states in XPS analysis of first row transition metals, oxides and hydroxides: Sc, Ti, V, Cu and Zn. *Appl. Surf. Sci.* **2010**, *257*, 887–898. [CrossRef]
41. Krishnan, P.; Liu, M.; Itty, P.A.; Liu, Z.; Rheinheimer, V.; Zhang, M.-H.; Monteiro, P.J.M.; Yu, L.E. Characterization of photocatalytic TiO_2 powder under varied environments using near ambient pressure X-ray photoelectron spectroscopy. *Sci. Rep.* **2017**, *7*, 43298. [CrossRef] [PubMed]
42. Kopanski, J.J.; Marchiando, J.F.; Lowney, J.R. Scanning capacitance microscopy applied to two-dimensional dopant profiling of semiconductors. *Mater. Sci. Eng. B.* **1997**, *44*, 46–51. [CrossRef]
43. Ruda, H.E.; Shik, A. Theoretical analysis of scanning capacitance microscopy. *Phys. Rev. B* **2003**, *67*, 235309. [CrossRef]
44. Fiorenza, P.; Alessandrino, M.S.; Carbone, B.; Russo, A.; Roccaforte, F.; Giannazzo, F. High-Resolution Two-Dimensional Imaging of the 4H-SiC MOSFET Channel by Scanning Capacitance Microscopy. *Nanomaterials* **2021**, *11*, 1626. [CrossRef] [PubMed]
45. Williams, C.C. Two-dimensional dopant profiling by scanning capacitance microscopy. *Annu. Rev. Mater. Sci.* **2003**, *29*, 471–504. [CrossRef]
46. Germs, W.C.; Adriaans, W.H.; Tripathi, A.K.; Roelofs, W.S.C.; Cobb, B.; Janssen, R.A.J.; Gelinck, G.H.; Kemerink, M. Charge transport in amorphous InGaZnO thin film transistors. *Phys. Rev. B* **2012**, *86*, 155319. [CrossRef]
47. Le, M.N.; Kim, H.; Kang, Y.K.; Song, Y.; Guo, X.; Ha, Y.G.; Kim, C.; Kim, M.G. Bulk charge-transfer doping of amorphous metal oxide: Fullerene blends for solution-processed amorphous indium zinc oxide thin-film transistors. *J. Mater. Chem. C* **2019**, *7*, 10635–10641. [CrossRef]
48. Waser, R.; Dittmann, R.; Staikov, G.; Szot, K. Redox-based resistive switching memories–nanoionic mechanisms, prospects, and challenges. *Adv. Mater.* **2009**, *21*, 2632–2663. [CrossRef] [PubMed]
49. Sarma, S.; Mothudi, B.M.; Dhlamini, S. Observed coexistence of memristive, memcapacitive and mmeminductive characteristics in polyvinyl alcohol/cadmium sulphide nanocomposites. *Mater. Sci. Mater. Electron.* **2016**, *27*, 4551. [CrossRef]
50. Sun, S.M.; Liu, W.J.; Wang, Y.P.; Huan, Y.W.; Ma, Q.; Zhu, B.; Wu, S.D.; Yu, W.J.; Horng, R.H.; Xia, C.T.; et al. Band alignment of $In_2O_3/\beta\text{-}Ga_2O_3$ interface determined by X-ray photoelectron spectroscopy. *Appl. Phys. Lett.* **2018**, *113*, 031603. [CrossRef]
51. Kraut, E.A.; Grant, R.W.; Waldrop, J.R.; Kowalczyk, S.P. Semiconductor core-level to valence-band maximum binding-energy differences: Precise determination by x-ray photoelectron spectroscopy. *Phys. Rev. B.* **1983**, *28*, 1965. [CrossRef]
52. Zawadzki, P.; Jacobsen, K.W.; Rossmeisl, J. Electronic hole localization in rutile and anatase TiO_2-self-interaction correction in Δ-SCF DFT. *Chem. Phys. Lett.* **2011**, *506*, 42–45. [CrossRef]
53. Zawadzki, P.; Rossmeisl, J.; Jacobsen, K.W. Electronic hole transfer in rutile and anatase TiO_2: Effect of a delocalization error in the density functional theory on the charge transfer barrier height. *Phys. Rev. B* **2011**, *84*, 121203. [CrossRef]
54. Zawadzki, P.; Jacobsen, K.W.; Dahl, S.; Rossmeis, J. Oxidative trends of TiO_2-hole trapping at anatase and rutile surfaces. *Energy Environ. Sci.* **2012**, *5*, 9866–9869. [CrossRef]
55. Jõgi, I.; Aarik, J.; Bichevin, V.; Käämbre, H.; Laan, M.; Sammelselg, V. Fowler–Nordheim tunneling in TiO_2 films grown by atomic layer deposition on gold substrates. *Proc. Est. Acad. Sci. Phys. Math.* **2004**, *53*, 226–236.
56. Aarik, J.; Bichevin, V.; Jogi, I.; Käämbre, H.; Laan, M.; Sammelselg, V. Fowler-Nordheim tunnelling in Au-TiO_2-Ag film structures. *Open Phys.* **2004**, *2*, 147–159. [CrossRef]

57. Chakraborty, S.; Bera, M.K.; Bhattacharya, S.; Maiti, C.K. Current conduction mechanism in TiO_2 gate dielectrics. *Microelectron. Eng.* **2005**, *81*, 188–193. [CrossRef]
58. Clerc, R.; Spinelli, A.; Ghibaudo, G.; Pananakakis, G. Theory of direct tunneling current in metal–oxide–semiconductor structures. *J. Appl. Phys.* **2002**, *91*, 1400–1409. [CrossRef]
59. Bratkovsky, A.M. Spintronic effects in metallic, semiconductor, metal–oxide and metal–semiconductor heterostructures. *Rep. Prog. Phys.* **2008**, *71*, 026502. [CrossRef]
60. Gao, Y.; Weston, A.; Enaldiev, V.; Li, X.; Wang, W.; Nunn, J.E.; Soltero, I.; Castanon, E.G.; Carl, A.; De Latour, H.; et al. Tunnel junctions based on interfacial two-*dimensional* ferroelectrics. *Nat. Commun.* **2024**, *15*, 4449. [CrossRef]

Disclaimer/Publisher's Note: The statements, opinions and data contained in all publications are solely those of the individual author(s) and contributor(s) and not of MDPI and/or the editor(s). MDPI and/or the editor(s) disclaim responsibility for any injury to people or property resulting from any ideas, methods, instructions or products referred to in the content.